Journal of Materials Science & Technology 89 (2021) 199–208

Contents lists available at ScienceDirect

Journal of Materials Science & Technology

journal homepage: www.jmst.org

Two-dimensional porous zinc cobalt sulfide nanosheet arrays with superior electrochemical performance for supercapatteries

Yang Li [a], Ziyang Luo [a], Shunfei Liang [a], Huizhen Qin [a], Xun Zhao [a], Lingyun Chen [a,*], Huayu Wang [a], Shaowei Chen [b,*]

[a] School of Chemistry and Chemical Engineering, Chongqing University, Chongqing 400044, China
[b] Department of Chemistry and Biochemistry, University of California, Santa Cruz, California 95060, United States

ARTICLE INFO

Article history:
Received 4 September 2020
Received in revised form 25 January 2021
Accepted 26 January 2021
Available online 9 April 2021

Keywords:
Two-dimensional materials
Porous nanosheet
Zinc cobalt sulfide
Supercapattery
Electrochemical energy storage

ABSTRACT

Unique two-dimensional (2D) porous nanosheets with overwhelmingly rich channels and large specific surface area exhibit superior electrochemical capacitance performance, as compared to the conventional zero- and one-dimensional counterparts. As ternary transition metal sulfides (TMSs) are well recognized for their high electrochemical activity and capacity, and the replacement of oxygen with sulfur may result in high stability and flexible properties of the nanomaterials, as compared to transition metal oxides, herein we report the synthesis of 2D porous nanosheet arrays of $Zn_xCo_{1-x}S$ (x = 0, 0.25, 0.5, 0.75, and 1) via a facile hydrothermal process. Due to the synergistic effect of the metal components and a unique 2D porous structure, the $Zn_{0.5}Co_{0.5}S$ electrode was found to stand out as the best among the series, with a high specific capacity of 614 C g^{-1} at 1 A g^{-1} and excellent cycle retention rate of 90 % over 10, 000 cycles at 10 A g^{-1}. Notably, a supercapattery based on a $Zn_{0.5}Co_{0.5}S$ positive electrode and an activated carbon (AC) negative electrode ($Zn_{0.5}Co_{0.5}S$//AC) was found to display a 1.6 V voltage window, a 61 mA h g^{-1} specific capacity at 1 A g^{-1}, a 49 Wh kg^{-1} energy density at 957 W kg^{-1} power density, and excellent cycling performance (88 % over 10, 000 cycles), suggesting tremendous potential of $Zn_{0.5}Co_{0.5}S$ in the development of high-performance supercapattery devices.

1. Introduction

Development of clean, efficient, and sustainable energy conversion/storage technologies has been stimulating extensive research interest, largely because of the potential applications in diverse areas, in particular, mobile electronics and transportation [1–3]. Among these, supercapacitors (SCs) represent an efficient and environmentally friendly technology, which features rapid charge-discharge dynamics, favorable power density, and extended cycle life [4,5]. At present, SCs are divided into two types based on charge storage mechanism. The first is electrical double layer capacitors (EDLC) that rely on non-faradaic charging/discharging of the electrode double layer, and the second is pseudocapacitors (PCs) based on faradaic reactions that occur on the electrode surface. Both EDLCs and PCs have the problem that the energy density (E) is much lower than that of batteries, which greatly limits their practical application potential and field. According to the calculation formula of energy density for capacitors ($E = 0.5CV^2$), the rational design of the positive and negative electrode configuration to broaden the overall working voltage (V) is helpful to improve the energy density of the capacitors. Hybrid supercapacitors (HSCs), also known as supercapatteries, which are assembled from electrode materials with two different storage mechanisms (e.g., EDLC on one electrode and PCs on the other) [6–9]. Supercapatteries represent a unique design by combining the characteristics of rechargeable batteries and supercapacitors, and are generally assembled using redox battery-type materials as one electrode and EDLC materials as the other electrode [10,11]. Notably, the energy/power density of supercapatteries can be readily manipulated by the design and engineering of the nanostructured electrode materials.

One commonly used material for electrodes of supercapatterie is transition metal oxides (TMOs), e.g., Co_3O_4 [12], NiO [13,14], MnO_2 [15], and ZnO [16]. Although TMOs exhibit a high specific capacitance and overwhelmingly rich Faraday redox reactions, the electrical conductivity and rate performance in general remain unsatisfactory. To mitigate the issues, bimetallic oxides, such as $NiCo_2O_4$ [17], $NiMn_2O_4$ [18], $CuFe_2O_4$ [19], and $CoMn_2O_4$ [20], have been used as electrode materials. Recently, transition metal sul-

* Corresponding authors.
E-mail addresses: lychen@cqu.edu.cn (L. Chen), shaowei@ucsc.edu (S. Chen).

https://doi.org/10.1016/j.jmst.2021.01.085
1005-0302/

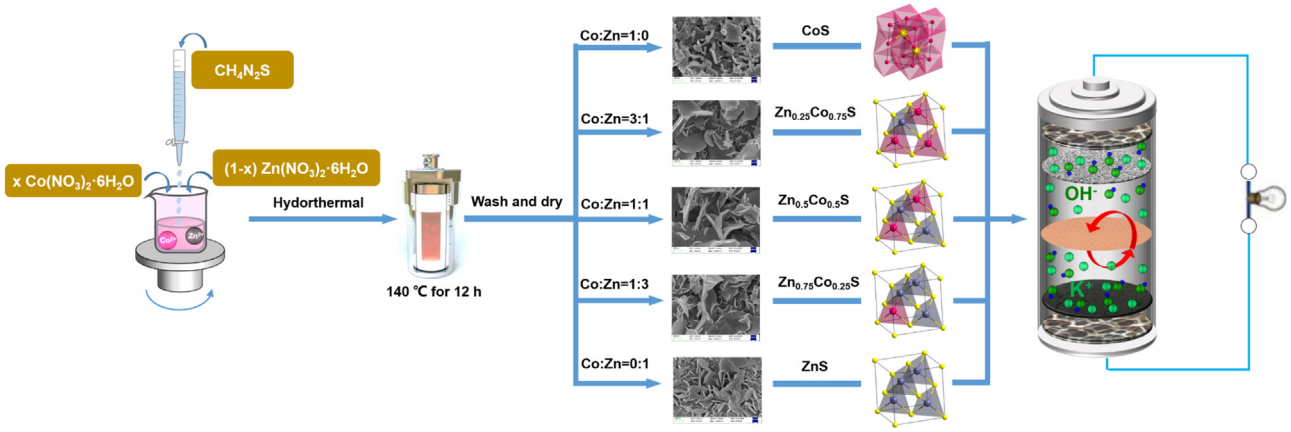

Scheme 1. Schematic of the synthetic procedure of $Zn_xCo_{1-x}S$.

fides (TMSs) have caught the attention of researchers in various fields, such as energy storage/conversion, solar cell, gas sensors, and nanoreactors, due to their unique physical and chemical properties, such as superior electrical conductivity and thermal stability [21–27]. Some supercapatteries have likewise been fabricated by using (TMSs) as electrode materials, such as CoS_2 [28], Ni_3S_2 [29], Co_9S_8 [30], and ZnS [31]. Compared to its oxide counterparts, TMSs present higher conductivity due to the replacement of oxygen with sulfur atoms produced a more flexible structure allowing easy electron transport lower electronegativity and lower band-gaps [32–34]. More recently, ternary TMSs, such as $NiCo_2S_4$ [35], $CoNiS_2$ [28], $MnCo_2S_4$ [36], and $FeNi_2S_4$ [37], have also been studied, due to the synergistic effect between the different metal species. Simultaneously, ternary TMSs have much lower optical band gap and much higher conductivity compared to their single TMSs counterparts [38]. For instance, zinc cobalt sulfide (ZnCoS) has been found to exhibit satisfactory electrochemical performance, due to its narrow optical band gap, ultrahigh electrical conductivity, and synergistic effect between the Co and Zn species [39]. For instance, Wu and co-workers [32] prepared hierarchical $Zn_{0.76}Co_{0.24}S$ flowers on nickel foam and observed a 1906 F g^{-1} specific capacitance at 1 A g^{-1}. In another study [40], $Zn_{0.76}Co_{0.24}S@Ni_3S_2$ core-shell nanosheets were synthesized on nickel foam, and exhibited a 1209 C g^{-1} specific capacitance at 2 A g^{-1}.

Herein, we report the preparation of porous ternary $Zn_xCo_{1-x}S$ (x = 0, 0.25, 0.5, 0.75, and 1.0) nanosheet arrays via a facile hydrothermal method that exhibit outstanding electrochemical performance, as compared to the individual sulfides. This is mainly ascribed to the following structural characteristics: (i) the unique 2D porous structure provides abundant channels for rapid mass transfer; (ii) the Co and Zn centers in the bimetallic compound provide rich redox reactions; and (iii) TMSs produce a softer structure than TMOs, because sulfur possesses a lower electronegativity than oxygen. Among the series of samples, $Zn_{0.5}Co_{0.5}S$ exhibits the highest specific capacitance and excellent cycle stability. A supercapattery device was assembled with $Zn_{0.5}Co_{0.5}S$ as the positive electrode and activated carbon (AC) as the negative electrode, which achieved an ultrahigh energy/power density and ultra-long cycle stability.

2. Experimental section

2.1. Materials

Thiourea (CH_4N_2S), cobalt nitrate hexahydrate ($Co(NO_3)_2·6H_2O$), zinc nitrate hexahydrate ($Zn(NO_3)_2·6H_2O$), potassium hydroxide (KOH) and polyvinylidene fluoride (PVDF) were purchased from Kelon in Chengdu, China. Foam nickel (NF) as a current collector was purchased from Jiayisheng Company. Commercial activated carbon (AC) was purchased from Nanjing Pioneer Nano Technology Co., Ltd. All chemicals were of analytical grade and used with no further purification.

2.2. Sample preparation

$Zn_xCo_{1-x}S$ samples were synthesized by a simple hydrothermal procedure (Scheme 1). Briefly, a solution was first prepared by dissolving $Zn(NO_3)_2$ and $Co(NO_3)_2$ (2 mmol each) in deionized water (40 mL) under magnetic stirring, and mixed with another solution containing 4 mmol of CH_4N_2S in 40 ml of deionized water under vigorous stirring. The resultant solution was then transferred into a Teflon-lined stainless steel autoclave (100 mL, Anhui Kemi Machinery Technology Co., Ltd.) and subject to hydrothermal treatment at 150 °C for 12 h. After the solution cooled down naturally to ambient temperature, the sample was rinsed with ethanol and deionized water multiple times, and dried at 60 °C in a vacuum oven for 24 h, affording $Zn_{0.5}Co_{0.5}S$ nanomaterials. $Zn_xCo_{1-x}S$ samples from other Zn/Co molar ratios (i.e., 1:0, 1:3, 3:1, and 0:1) were also synthesized in the same manner.

2.3. Characterizations

Scanning electron microscopy (SEM) studies were carried out with a HITACHI S-4800 field-emission scanning electron microscope (FESEM), and transmission electron microscopy (TEM) studies with a Tecnai G2 F20 S-Twin microscope operated at 200 kV. X-ray diffraction (XRD) and X-ray photoelectron spectroscopic (XPS) studies were performed with a Bruker D8 Advance powder diffractometer and an ESCALAB250Xi spectrometer, respectively. Nitrogen adsorption-desorption isotherms were acquired with a Micromeritics ASAP 2020 analyzer.

2.4. Electrochemical performance

Half-cell measurements were conducted in a three-electrode configuration with an aqueous solution of 2 M KOH with a CHI 760E electrochemical workstation, using a saturated calomel electrode (SCE) as the reference electrode and a platinum mesh as the counter electrode. To prepare the working electrode, the $Zn_xCo_{1-x}S$ obtained above, acetylene black and PVDF were dissolved in N-methyl 2-pyrrolidinone (NMP) at the respective mass fraction of 80 %, 10 %, and 10 %, and the uniformly mixed slurry was deposited onto a piece of nickel foam (1 cm × 1 cm) and fixed by a motor clamp, corresponding to a $Zn_xCo_{1-x}S$ loading of ca. 1.5 mg cm^{-2}.

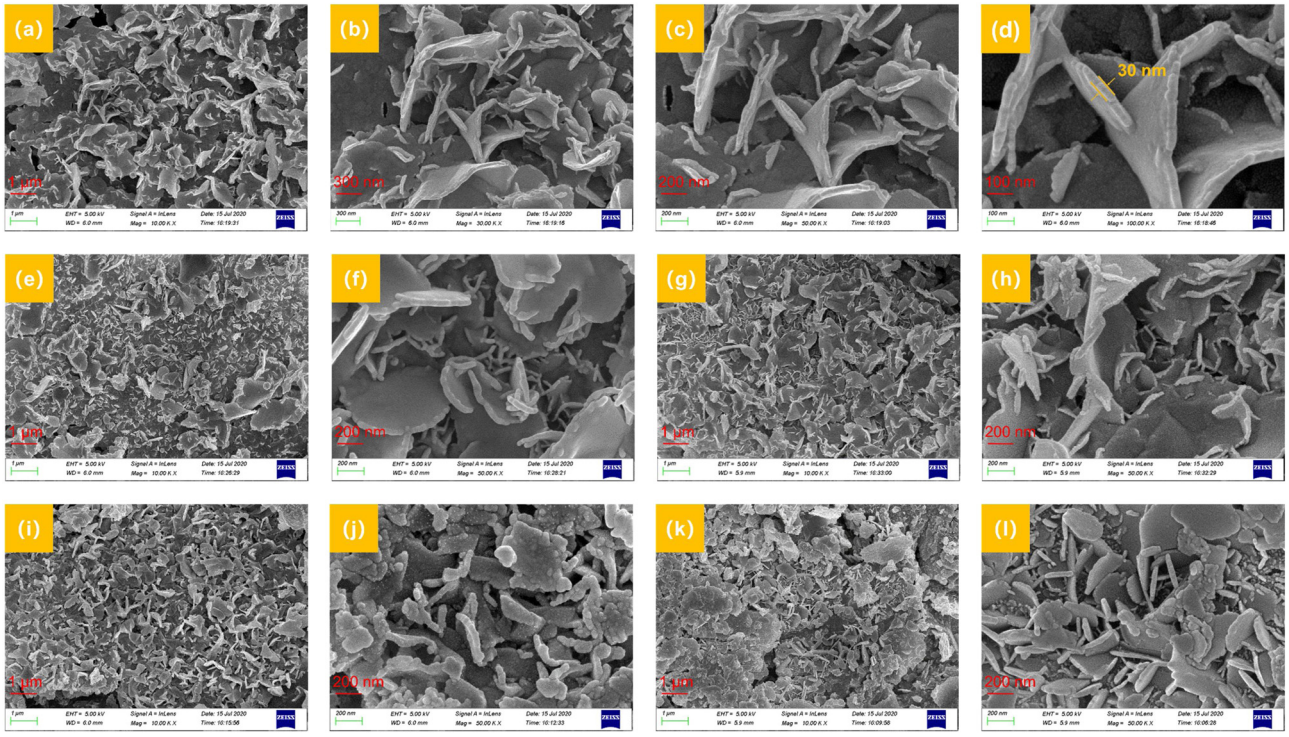

Fig. 1. Representative SEM images of (a-d) $Zn_{0.5}Co_{0.5}S$, (e-f) $Zn_{0.25}Co_{0.75}S$, (g-h) $Zn_{0.75}Co_{0.25}S$, (i-j) CoS, and (k-l) ZnS nanosheets.

Impedance measurements were carried out at the open-circuit voltage with the frequency varied from 0.01 Hz to 100 kHz. Cycling stability of the active materials was evaluated using a LANHE test equipment. The specific gravimetric capacity (Q, C g^{-1}) of the electrode was estimated by Eq. (1) [41],

$$Q = \frac{2I\int V\mathrm{d}t}{m\Delta V} \tag{1}$$

with I being the electrode current, ΔV the fixed potential range, m the content of the active material on the NF, and $\int V{\cdot}dt$ the integral area under the discharge curve.

2.5. Cell performance measurements

A supercapattery device was assembled consisting of a $Zn_xCo_{1-x}S$ anode and a commercial AC cathode. Full-cell tests were implemented in a two-electrode configuration with a CHI 760E Electrochemical Workstation in 2 M KOH in water. The optimal ratio of the mass loadings between $Zn_xCo_{1-x}S$ (m^+) and AC (m^-) was determined by Eq. (2),

$$\frac{m^+}{m^-} = \frac{C^- \times \Delta V^-}{C^+ \times \Delta V^+} \tag{2}$$

where C is the specific capacitance, and V the potential window. Three parameters were used to quantify the performance of the supercapattery, specific capacity (C_s, mAh g^{-1}), energy density (E, Wh kg^{-1}), and power density (P, W kg^{-1}) [42],

$$C_s = \frac{2I\int V\mathrm{d}t}{3.6\,m\Delta V} \tag{3}$$

$$E = \frac{I\int V\mathrm{d}t}{3.6m} \tag{4}$$

$$P = \frac{3600 \times E}{\Delta t} \tag{5}$$

where I, m, t, ΔV and $\int V{\cdot}dt$ represent the current, combined mass loading of the anode and cathode active materials, discharge time, potential window, and the integrated area enclosed by the discharge curve, respectively.

3. Results and discussion

A series of $Zn_xCo_{1-x}S$ (x = 0, 0.25, 0.5, 0.75, and 1) nanosheet arrays were prepared by a facile hydrothermal procedure at 150 °C at controlled $Zn(NO_3)_2/Co(NO_3)_2$ feed ratios along with thiourea. The structures of the $Zn_xCo_{1-x}S$ nanosheets were first characterized by SEM and TEM measurements. From the low-magnification SEM images in Fig. 1(a, b), the $Zn_{0.5}Co_{0.5}S$ sample can be seen to display a 2D nanosheet array structure, which entailed a uniform porous nanostructure formed by the disorderly stacking of many fine nanosheets of about 30 nm in thickness, as revealed in high-resolution SEM images (Fig. 1(c, d)). $Zn_xCo_{1-x}S$ samples prepared at other Zn/Co atomic ratios showed a similar 2D porous nanosheet structure (Figs. 1(e)-(l) and S1). The porous nanosheet structure of the $Zn_{0.5}Co_{0.5}S$ sample can also be seen in TEM studies (Fig. 2(a)), which was composed of a large number of flakes. High-resolution TEM studies (Fig. 2(b)) clearly show the formation of ultra-thin, wrinkled nanosheets of about 30 nm in thickness. From the selected area electron diffraction (SAED) patterns (Fig. 2(c) inset), the lattice spacing was quantified to be 0.31, 0.19, and 0.16 nm, corresponding to the (111), (220), and (311) facets of $Zn_{0.5}Co_{0.5}S$ (JCPDS No.47–1656). The lattice fringes can also be clearly resolved in high-magnification TEM measurements (Fig. 2(c)), where the interplanar distances of 0.31 nm and 0.19 nm were readily resolved. Fig. 2(d)-(k) shows the TEM images of other samples in the series, which exhibited similar morphology and structure.

XRD measurements were then carried out to further characterize the obtained samples. From Fig. 3(a), the $Zn_xCo_{1-x}S$ (x = 0.25, 0.5, 0.75, and 1) samples can be seen to display three major peaks at 2θ = 29.0°, 48.1°, and 57.1°, which can be ascribed to the (111), (220), and (311) diffractions of $Zn_{0.76}Co_{0.24}S$ (JCPDS No. 47-1656, with lattice constants of $a = b = c$ =5.39 Å) and ZnS (JCPDS No. 05-

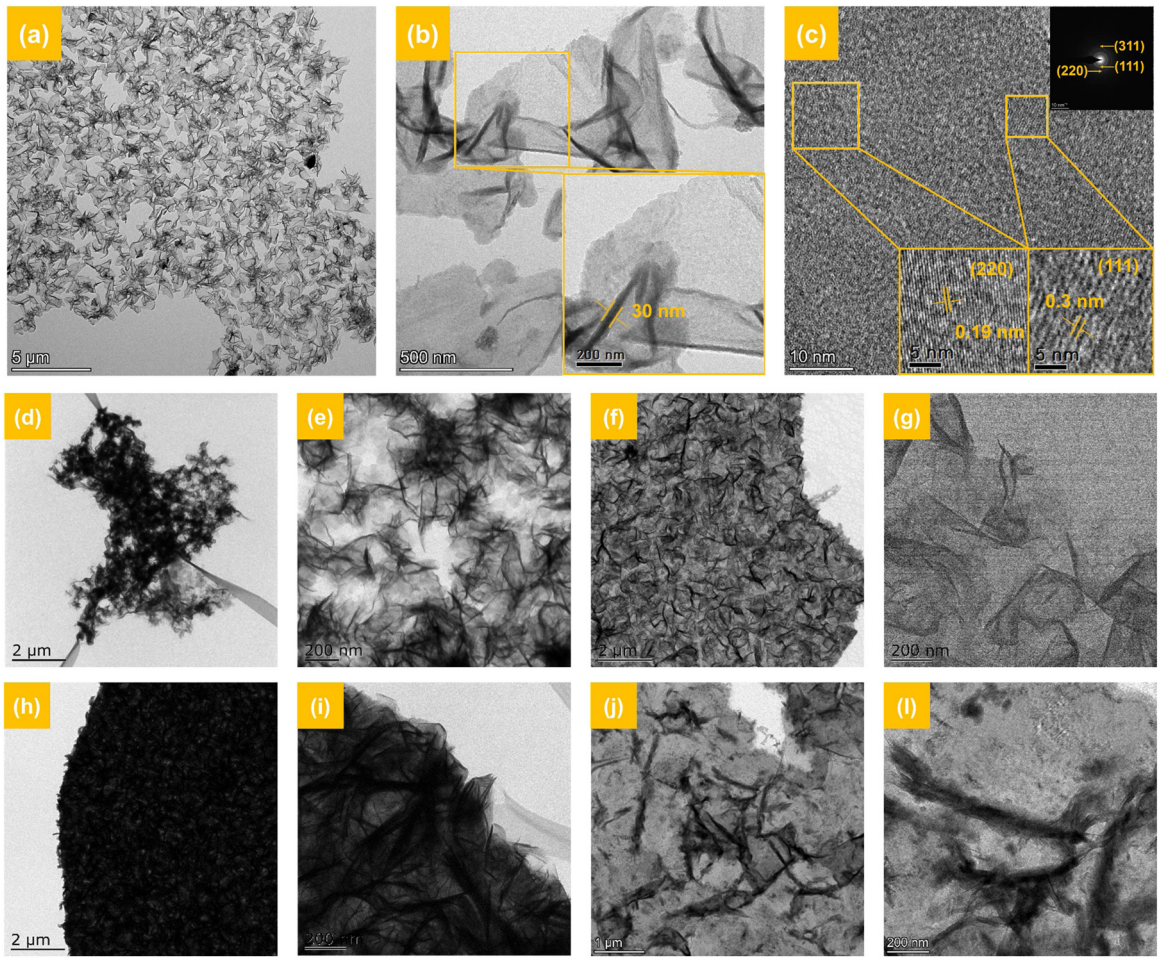

Fig. 2. TEM images of (a-c) $Zn_{0.5}Co_{0.5}S$, (d, e) $Zn_{0.25}Co_{0.75}S$, (f, g) $Zn_{0.75}Co_{0.25}S$, (h, i) CoS, and (j, k) ZnS nanosheets. Panel (b) inset is a zoom in of the boxed area. Top inset to panel (c) is the corresponding SAED patterns, and the bottom insets are the zoom in of the boxed areas.

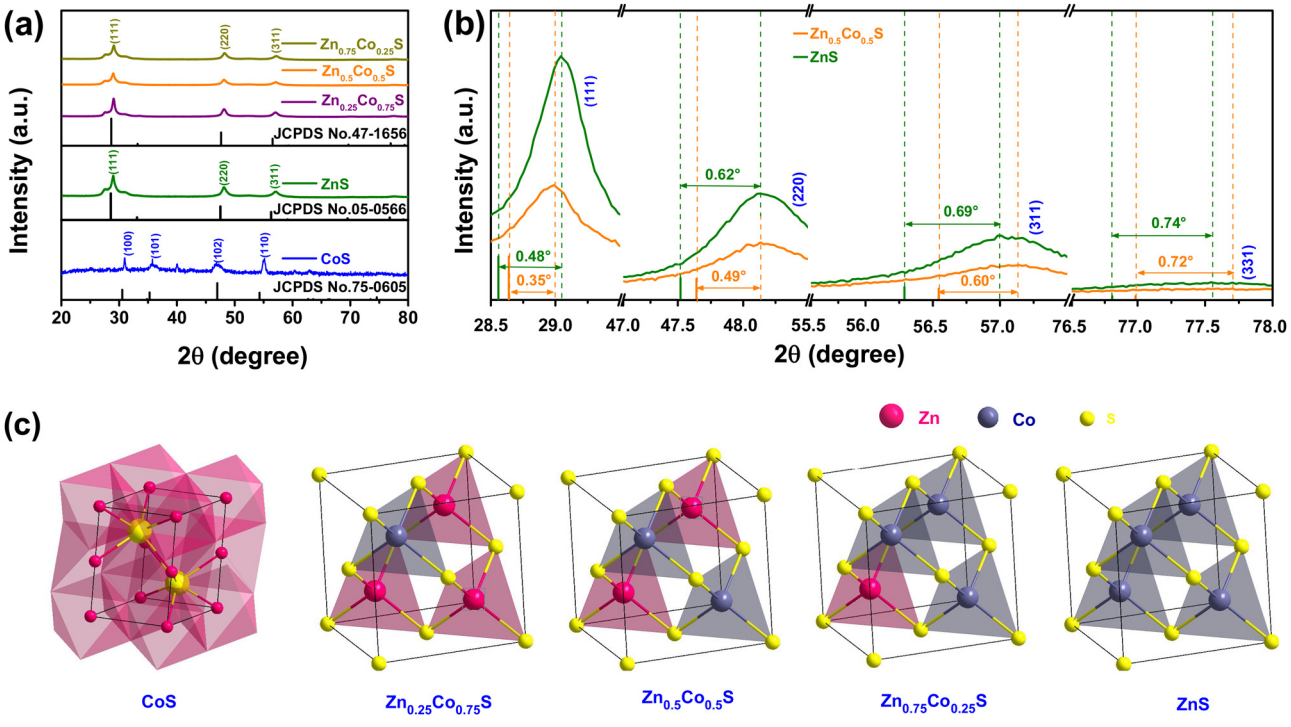

Fig. 3. (a, b) XRD patterns and (c) crystal structure diagram of the $Zn_xCo_{1-x}S$ nanosheets.

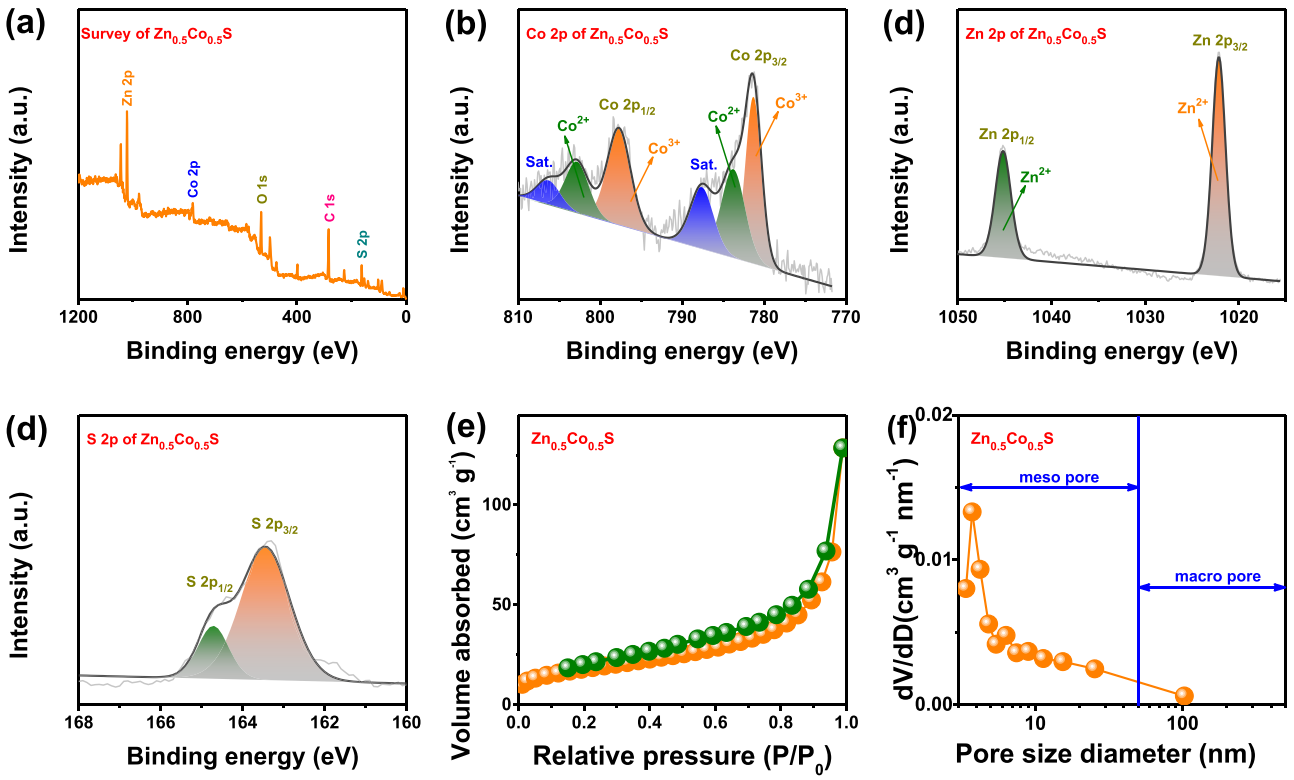

Fig. 4. (a) Full-survey spectrum of $Zn_{0.5}Co_{0.5}S$ nanosheets, and the corresponding high-resolution XPS scans of the (b) Co 2p, (c) Zn 2p, and (d) S 2p electrons. (e) N_2 adsorption-desorption isotherm and (f) pore size distribution of $Zn_{0.5}Co_{0.5}S$ nanosheets.

0566, with lattice constants of $a = b = c$ =5.41 Å) with F-m43 group symmetry [43,44]. Additional diffraction peaks can be seen at 2θ = 30.9° (100), 35.7° (101), 47.2° (102), and 54.9° (110) for CoS (JCPDS No.75−0605, with lattice constants of $a = b$ =3.38 Å and c =5.15 Å) with P63/mmc group symmetry, respectively [45]. One can see that the position and intensity of the diffraction peaks of $Zn_xCo_{1-x}S$ are very close to those of ZnS, suggesting a similar crystalline lattice. It is well known that the ionic radius of Zn^{2+} (74 pm) is only marginally larger than those of Co^{2+} and Co^{3+} (74 vs. 69 and 61 pm). Therefore, it is most likely that $Zn_xCo_{1-x}S$ (x = 0.25, 0.5, and 0.75) nanosheets were synthesized by the replacement of Zn^{2+} in ZnS with Co^{2+}/Co^{3+} [45]. Compared with the standard diffraction patterns, the diffraction peaks of ZnS and $Zn_{0.5}Co_{0.5}S$ nanosheets (Fig. 3(b)) can be found to shift to a higher angle, suggesting macroscopic residual stress inside the materials (rather than the error of the instrument) [46,47]. In addition, all the diffraction peaks of ZnS appear at a larger angle than those of $Zn_{0.5}Co_{0.5}S$, indicating that Co ions successfully replaced Zn ions in ZnS. Due to the inclusion of heteroatoms that were smaller than the host atoms, the lattice constants became smaller and the XRD diffraction peaks shifted to a larger angle. Fig. 3(c) shows the crystal structure of $Zn_xCo_{1-x}S$. The interplanar spacing (d) of $Zn_{0.5}Co_{0.5}S$ was estimated by the Bragg equation,

$$2d\sin\theta = n\lambda (n = 1, 2, 3\ldots) \quad (6)$$

where θ, n, and λ denote the diffraction angle, reflection order (n = 1, 2, 3, …), and X-ray wavelength (λ =0.15406 nm). Based on Eq. (6), the interplanar spacings of the diffraction peaks at 2θ = 29.0°, 48.1°, and 57.1° were estimated to be 0.31, 0.19 and 0.16 nm, respectively, consistent with results from TEM measurements (Fig. 2). These results show that the $Zn_xCo_{1-x}S$ samples were indeed successfully synthesized.

The valence states and surface elemental composition of the $Zn_xCo_{1-x}S$ nanosheets were then analyzed by XPS studies. Fig. 4(a) shows the full spectrum of the $Zn_{0.5}Co_{0.5}S$ nanosheets, where the elements of Zn (1022 eV), Co (781 eV), and S (163 eV) can be clearly resolved (the C signals at 284 eV and O at 531 eV most likely arose from H_2O and CO_2 impurities) [48]. Deconvolution of the high–resolution scan of the Co 2p electrons (Fig. 4(b)) yields two doublets at the binding energies of $2p_{3/2}/2p_{1/2}$ = 781.2/797.1 eV for Co^{3+} and 782.7/798.9 eV for Co^{2+}, along with two satellite peaks (787.4 and 803.6 eV) [39] The high-resolution scan of the Zn 2p electrons (Fig. 4(c)) entails two main peaks at 1022.2 and 1045.2 eV, due to the $2p_{3/2}$ and $2p_{1/2}$ electrons of Zn^{2+}, respectively [49]. Similarly, deconvolution of the S 2p high-resolution spectrum (Fig. 4(d)) yielded two peaks at ($2p_{3/2}$) 163.5 and ($2p_{1/2}$) 164.7 eV of S^{2-} [50]. Additionally, from the integrated peak area, the atomic ratio of Zn/Co in the $Zn_{0.5}Co_{0.5}S$ sample can be estimated to be 1.2, close to the initial feed ratio.

The porosity of the $Zn_xCo_{1-x}S$ nanosheets was then examined by nitrogen adsorption-desorption analysis. The $Zn_{0.5}Co_{0.5}S$ sample can be seen to display a type IV isotherm with an obvious H3 hysteresis loop (Fig. 4(e)), suggesting the formation of mesopores and capillary condensation in the material [51]. Fig. 4(f) shows the distribution curve of the pore size based on the Barrett-Joyner-Halenda (BJH) model, where the pore size of the $Zn_{0.5}Co_{0.5}S$ sample is mainly distributed between 3 and 50 nm, suggesting the absence of macropores and micropores. The specific surface area of the $Zn_{0.5}Co_{0.5}S$ nanosheets was estimated to be 43.64 $m^2\ g^{-1}$, average pore diameter 3.71 nm, and pore volume 0.18 $m^3\ g^{-1}$, a unique feature conducive to the electrochemical capacitance performance.

The half-cell electrochemical tests of the prepared samples were then conducted in a three-electrode set-up in a water solution of 2 M KOH. Fig. 5(a) shows the CV curves of the $Zn_xCo_{1-x}S$ electrodes at the potential sweep rate of 40 mV s^{-1} in 0 to 0.6 V (vs. SCE). All samples can be seen to display a pair of voltamme-

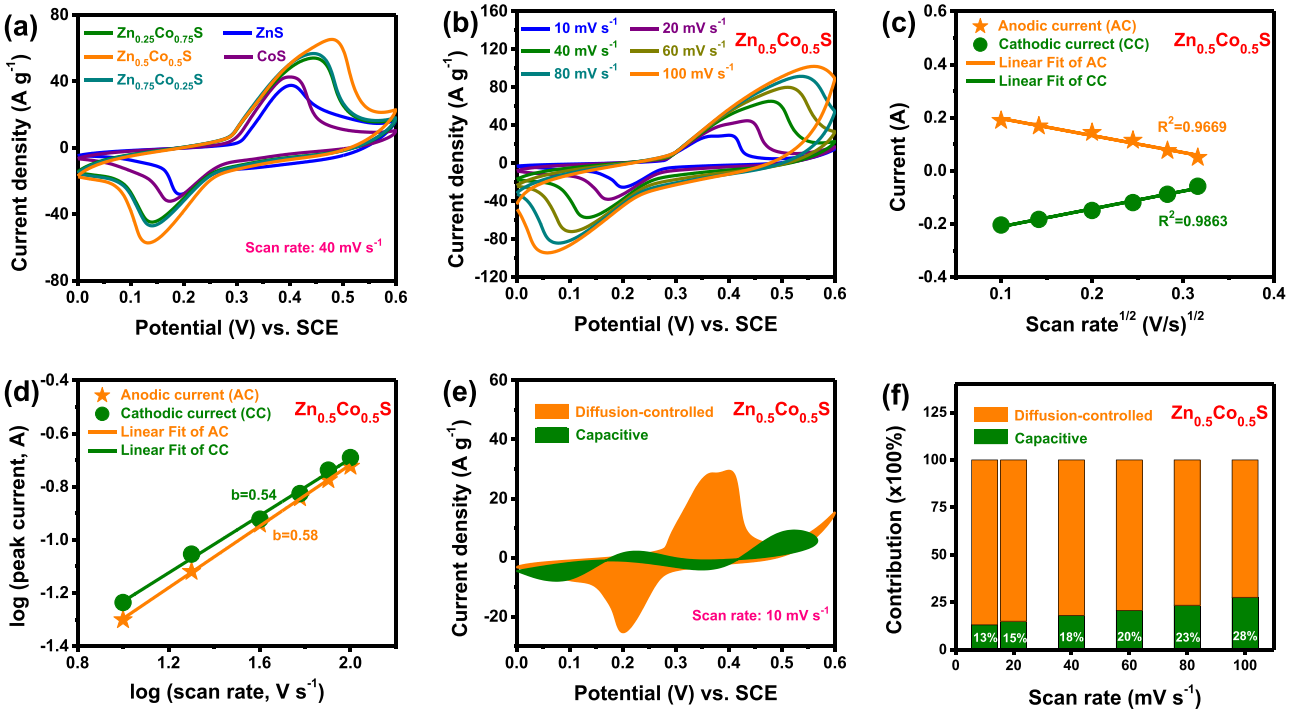

Fig. 5. (a) CV curves of the $Zn_xCo_{1-x}S$ nanosheets at the potential sweep rate of 40 mV s^{-1}. (b) CV curves of the $Zn_{0.5}Co_{0.5}S$ nanosheets with the potential sweep rate varied from 10 to 100 mV s^{-1}. (c) Plot of cathodic and anodic peak currents of the $Zn_{0.5}Co_{0.5}S$ electrode with the square root of the potential sweep rate. (d) Linear regressions of log (i) and log (v) of the $Zn_{0.5}Co_{0.5}S$ electrode. (e) Capacitive and diffusion-controlled contributions to the total current of the $Zn_{0.5}Co_{0.5}S$ electrode at 10 mV s^{-1}. (f) Fraction of the capacitive contribution of the $Zn_{0.5}Co_{0.5}S$ electrode at various potential sweep rates.

try peaks, most likely arising from battery-type Faraday reactions [44],

$$ZnS + OH^- \leftrightarrow ZnSOH + e^- \quad (7)$$

$$CoS + OH^- \leftrightarrow CoSOH + e^- \quad (8)$$

$$Zn_xCo_{1-x}S + OH^- \leftrightarrow xZnSOH + (1-x)CoSOH + e^- \quad (9)$$

$$CoSOH + OH^- \leftrightarrow CoSO + H_2O + e^- \quad (10)$$

Notably, the peak current and integral area of the CV curves of the $Zn_{0.5}Co_{0.5}S$ electrode are significantly greater than those of the other four samples. This means that the $Zn_{0.5}Co_{0.5}S$ electrode has a more active redox reaction and a higher capacity, which likely arose from the synergistic interactions within the multi-metallic system [39]. From Fig. 5(b), one can see virtually no change of the shape of the CV curve when the potential sweep rate is increased from 10 to 100 mV s^{-1}. This indicates that the $Zn_{0.5}Co_{0.5}S$ electrode has excellent reversibility and rate performance. In addition, at increasing scan rates, the anode and cathode peaks shift only slightly to the positive and negative directions, indicative of low charge-transfer resistance and fast redox reactions of the $Zn_{0.5}Co_{0.5}S$ electrode, in comparison to other electrodes (Fig. S2). Fig. 5(c) shows the linear regression of the peak current (i) and the square root of the potential sweep rate ($v^{1/2}$). It can be seen from the fitting in the figure that the electrochemical current of the sample is diffusion-controlled.

To study the dynamics of the $Zn_{0.5}Co_{0.5}S$ electrode, the dependence of the peak current (i) on the corresponding scan rate (v) can be expressed by Eq. (11) [52],

$$i = av^b \quad (11)$$

with a and b being fitting constants. b also represents the reaction kinetics,

$$b = \frac{\log i - \log a}{\log v} = \frac{\log i}{\log v} - \log_v a \, (cons\tan ts)\square \quad (12)$$

At b = 1, the energy storage is controlled by the surface capacitance; whereas at b = 0.5, it suggests a diffusion-controlled process [53]. According to the linear relationship (Fig. 5(d)), the b value was estimated to be 0.58 for the anodic sweep and 0.54 for the cathodic sweep, which implies that charge storage is largely determined by diffusion-controlled Faraday processes and capacitance effects. These two contributions can be quantified by Eqs. (13) or (14) [52],

$$i(v) = k_1 v + k_2 v^{1/2} \quad (13)$$

$$i(v)/v^{1/2} = k_1 v^{1/2} + k_2 \quad (14)$$

Fig. 5(e) shows that approximately 42 % of the charge storage at the potential sweep rate of 10 mV s^{-1} arose from the diffusion-controlled process. At increasing potential sweep rate, the capacitance contribution increases accordingly, whereas the diffusion-controlled component diminishes (Fig. 5(f)). This verifies that the capacitive effects are dominant at high scan rates.

Fig. 6(a) presents the galvanostatic charge-discharge (GCD) profiles of the $Zn_xCo_{1-x}S$ electrodes at 4 A g^{-1} current density, which all show a clear charge-discharge platform at 0 to 0.45 V. This is completely different from the isosceles triangle shape characteristic of a conventional EDLC [54]. This result indicates that Faraday reactions indeed occurred at the three electrodes (Eqs. 7–10). In addition, the $Zn_{0.5}Co_{0.5}S$ electrode shows a longer charge-discharge time and a greater integrated area under the discharge curve at the same current density (4 A g^{-1}) and potential window (0 to 0.45 V) than the other electrodes, suggesting a larger specific capacitance for the $Zn_{0.5}Co_{0.5}S$ electrode. Fig. 6(b) shows the GCD curves of the $Zn_{0.5}Co_{0.5}S$ electrode with the current density varied from 1 to 10 A g^{-1}, and Q (Fig. 6(c)) was calculated to be 614 C g^{-1} at the current density of 1 A g^{-1}, 584 C g^{-1} at 2 A g^{-1}, 551 C g^{-1} at 4 A g^{-1}, 526 C g^{-1} at 6 A g^{-1}, 500 C g^{-1} at 8 A g^{-1} and 478 C g^{-1} at 10 A g^{-1}. A decrease of the specific capacitance of the electrode can be seen with an increase of the current density, likely thanks to the concentration

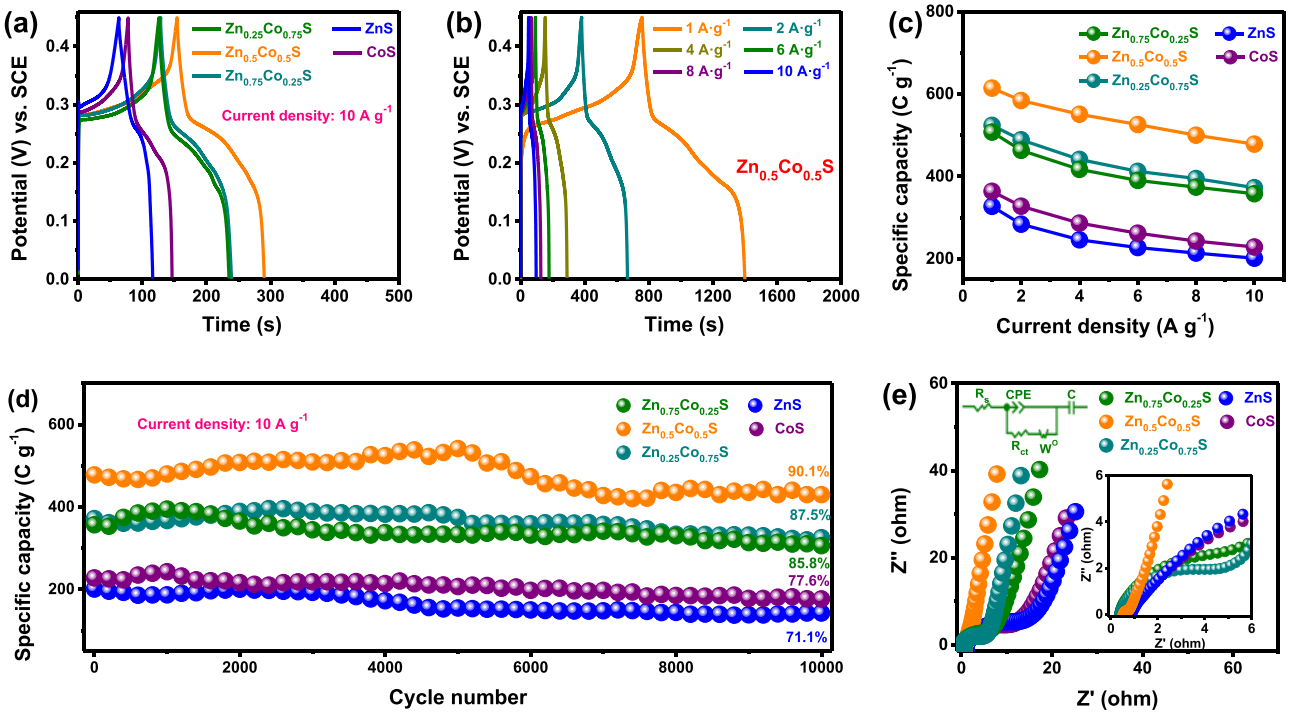

Fig. 6. (a) GCD profiles of the $Zn_xCo_{1-x}S$ nanosheets at the 4 A g^{-1} fixed current density. (b) GCD curves of the $Zn_{0.5}Co_{0.5}S$ nanosheets at 1 to 10 A g^{-1}. (c) Comparison of the specific capacity of the $Zn_xCo_{1-x}S$ electrodes at various current densities. (d) Specific capacity over 10, 000 GCD cycles at 10 A g^{-1}, and (e) Nyquist plots of the $Zn_xCo_{1-x}S$ electrodes. Top inset to panel (e) is the equivalent circuit, whereas the bottom inset is a zoom in of the low-impedance region.

polarization effect of the electrode, so that the active material cannot fully facilitate the redox reaction [44]. The GCD curves of the other electrodes were included in Fig. S3, and the corresponding Q was calculated and included in Fig. 6(c). At the current density of 10 A g^{-1}, the ZnS, $Zn_{0.75}Co_{0.25}S$, $Zn_{0.5}Co_{0.5}S$, $Zn_{0.25}Co_{0.75}S$, and CoS electrodes can be seen to still retain 62 %, 71 %, 78 %, 71 %, and 63 % of the mass specific capacitance at 1 A g^{-1}, respectively, indicating excellent rate performance.

Long-term stability is a key parameter for the safe operation and service life of the electrodes in practical applications. Therefore, the cycle stability of the $Zn_xCo_{1-x}S$ samples was tested by repeated GCD measurements at 10 A g^{-1}. From Fig. 6(d), the capacity retention rates of the ZnS, $Zn_{0.75}Co_{0.25}S$, $Zn_{0.5}Co_{0.5}S$, $Zn_{0.25}Co_{0.75}S$, and CoS electrodes after 10, 000 cycles were determined to be 71 %, 86 %, 90 %, 88 %, and 78 %, respectively, indicating outstanding cycle stability. Additionally, the $Zn_{0.5}Co_{0.5}S$ electrode shows better cycle stability than the other electrodes. One may notice that the capacity of these electrodes increased slightly during the first few thousands of charge-discharge cycles, and then gradually decreased, suggestive of activation of the electrode materials in the initial scans [44,53]. Notably, in comparison with TMSs and TMOs reported recently in the literature, the $Zn_{0.5}Co_{0.5}S$ electrode can be seen to exhibit an outstanding electrochemical performance (Table S1).

Electrochemical impedance spectroscopy (EIS) measurements were then conducted to further explore the charge transfer kinetics and the results were compared. Fig. 6(e) shows the Nyquist plots of the $Zn_xCo_{1-x}S$ electrodes at the open-circuit voltage in the frequency range of 0.01 Hz to 100 kHz. From the fitting of the EIS data (the corresponding equivalent circuit is depicted in the top inset to Fig. 6(e)), the charge transfer resistances (R_{ct}) was estimated to be 6.64 Ω for ZnS, 3.31 Ω for $Zn_{0.75}Co_{0.25}S$, 0.13 Ω for $Zn_{0.5}Co_{0.5}S$, 3.58 Ω for $Zn_{0.25}Co_{0.75}S$, and 5.12 Ω for CoS, with a respective solution resistance (R_s) of 1.13, 0.58, 0.55, 0.57 and 0.99 Ω. That is, $Zn_{0.5}Co_{0.5}S$ exhibited the lowest charge-transfer resistance among the series. Furthermore, at low frequencies, the linear segment of $Zn_{0.5}Co_{0.5}S$ exhibited a greater slope than those of the other samples, indicating a faster diffusion rate of OH^- [55,56]. Taken together, these observations are consistent with results from the GCD and CV tests, where the $Zn_{0.5}Co_{0.5}S$ sample exhibited the best performance among the series.

The high performance of the $Zn_{0.5}Co_{0.5}S$ electrode may be due to the following structural characteristics. (i) 2D porous nanosheets with a rich pore structure and large electrochemical surface area provide ready accessibility of a large number of reaction active sites. (ii) CoS and ZnS have a similar crystal structure, and the chemical properties of Co and Zn atoms are very similar, which makes it possible to form bimetallic sulfide and enhance the electrochemical properties due to the synergistic effect of the metal centers. (iii) Ternary transition metal sulfides have high electrochemical activity and capacity due to redox reactions caused by various oxidation states and high electrical conductivity. It is also highly stable and flexible, as compared to metal oxides because sulfur is less electronegative than oxygen.

To assess the practical application of the samples, $Zn_xCo_{1-x}S$//AC supercapattery devices were assembled by using the $Zn_xCo_{1-x}S$ nanosheets (with a battery-type energy storage mechanism) as the positive electrode ($Zn_xCo_{1-x}S$/NF) and AC (with an electric double-layer energy storage mechanism) as the negative electrode (AC/NF) in 2 M KOH in water (Fig. 7(a)). The supercapacitor energy density ($E = 0.5CV^2$) can be improved by increasing the capacitance (C) per unit mass and the working potential window (V) of the samples. Therefore, the capacitive properties of the AC electrode were also assessed in a three-electrode configuration. From Fig. S4(a), all CV curves can be seen to show a rectangular shape at potential sweep rates up to 100 mV s^{-1}, which is consistent with the capacitance characteristics of the electrical double-layer energy storage mechanism [57]. The corresponding GCD curves (Fig. S4(b)) do not show a charge-discharge platform at current densities up to 10 A g^{-1} in the potential range of -1 to 0 V. Based on these data, the AC electrode was found to exhibit a specific capacitance of 133 C g^{-1} at 1

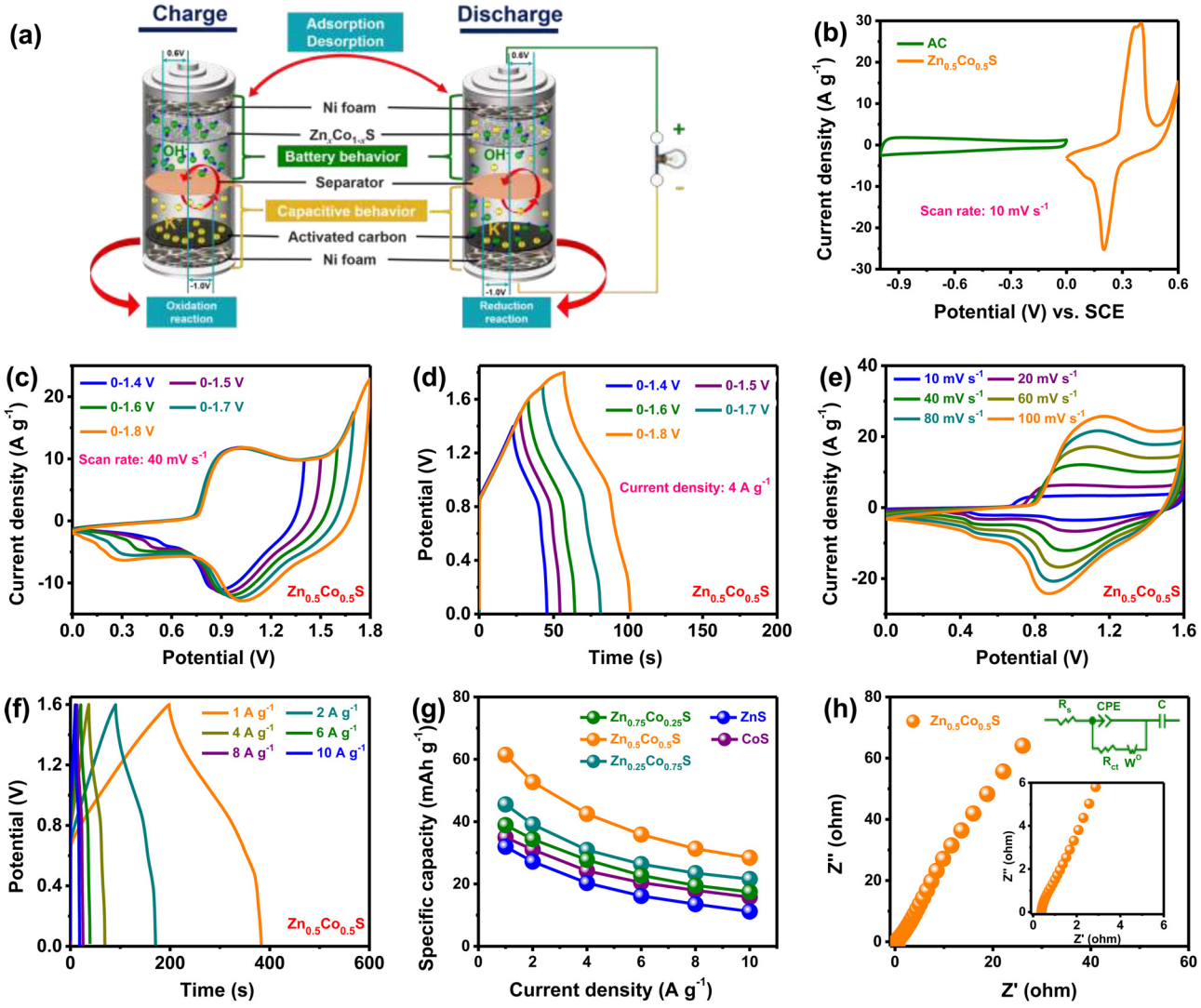

Fig. 7. (a) Structural schematic of the $Zn_xCo_{1-x}S$//AC supercapattery. (b) CV curves of the $Zn_{0.5}Co_{0.5}S$ and AC electrodes at the fixed potential sweep rate of 10 mV s^{-1}. (c) CV curves at the potential sweep rate of 40 mV s^{-1} and (d) GCD profiles at 4 A g^{-1} current density of the $Zn_{0.5}Co_{0.5}S$//AC supercapattery in varied potential windows. (e) CV at different potential sweep rates and (f) GCD profiles at different current densities of the $Zn_{0.5}Co_{0.5}S$//AC supercapattery. (g) Variation of the specific capacitance of the $Zn_xCo_{1-x}S$//AC supercapatteries with current density. (h) Nyquist plots of the $Zn_{0.5}Co_{0.5}S$//AC supercapattery. Insets to panel (h) are (top) equivalent circuit and (bottom) zoom in of the low-impedance region.

A g^{-1}, 126 C g^{-1} at 2 A g^{-1}, 119 C g^{-1} at 4 A g^{-1}, 112 C g^{-1} at 6 A g^{-1}, 108 C g^{-1} at 8 A g^{-1}, and 107 C g^{-1} at 10 A g^{-1} (Fig. S4(c)). Therefore, the optimal mass ratio between $Zn_{0.5}Co_{0.5}S$ and AC in the supercapattery was calculated to be 0.36 at 1 A g^{-1} current density (details in the Supporting Information). Therefore, the actual mass loadings of the active material and AC were fixed at 1.5 and 4.2 mg cm^{-2}, respectively.

Fig. 7(b) depicts the CV profiles of the $Zn_{0.5}Co_{0.5}S$ and AC electrodes at the potential sweep rate 10 mV s^{-1}. With a potential window of 0 to 0.6 V for the $Zn_{0.5}Co_{0.5}S$ electrode and -1 to 0 V for the AC electrode, the range of potential of the $Z_{0.5}C_{0.5}S$//AC supercapattery was set at 0–1.6 V. This is confirmed in two tests. Fig. 7(c) shows the CV curves of the supercapattery at the potential sweep rate of 40 mV s^{-1} within various potential ranges. At potentials beyond 1.7 V, the device began to produce polarization. Subsequently, the GCD profiles of the supercapattery were collected at 4 A g^{-1} in various potential windows (Fig. 7(d)). When the charging voltage exceeded 1.6 V, it was sometimes difficult to increase the voltage while continuing to charge the device. Based on the above results, the final potential window of the $Zn_{0.5}Co_{0.5}S$//AC supercapattery was set at 0–1.6 V, and CV curves were obtained at different scan rates (Fig. 7(e)), which are composed of a narrow curves (0 to 0.8 V) with a low current response and broad curves (0.8–1.6 V) with symmetrical peaks, featuring both capacitance and battery-type behaviors [58,59].

At increasing sweep rate, the CV curves did not show a significant change of the shape, indicating high electrochemical reversibility and excellent rate performance of the supercapattery. In fact, all GCD curves (1–10 A g^{-1}) of the device are neither triangular nor obvious charge-discharge platforms (Fig. 7(f)), suggesting combined contributions of two capacitor types, in good agreement with the CV results [60]. The device was found to exhibit a specific capacity (C) of 61 mA h g^{-1} at 1 A g^{-1}, 53 mA h g^{-1} at 2 A g^{-1}, 42 mA h g^{-1} at 4 A g^{-1}, 36 mA h g^{-1} at 6 A g^{-1}, 31 mA h g^{-1} at 8 A g^{-1}, and 28 mA h g^{-1} at 10 A g^{-1}. The electrochemical data of supercapatteries based on other $Zn_xCo_{1-x}S$ electrodes are shown in Fig. S5, which are consistent with the characteristics of the $Zn_{0.5}Co_{0.5}S$//AC device. Additionally, to compare their electrochemical performance, the C values of these devices were estimated at different current den-

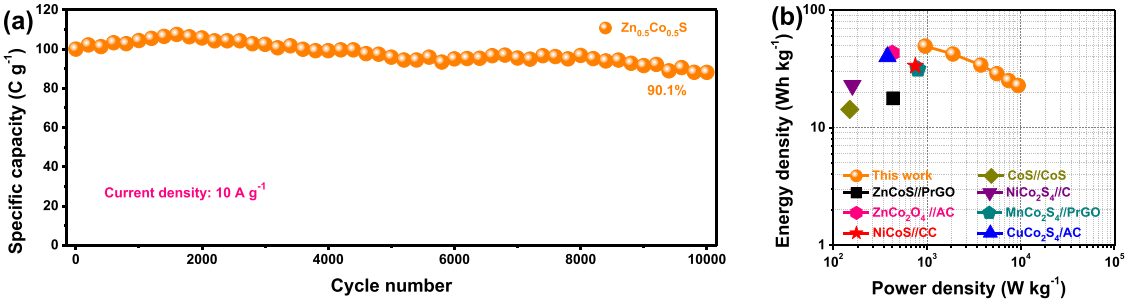

Fig. 8. (a) Reversibility tests of 10, 000 GCD cycles at 10 A g^{-1} of the $Zn_{0.5}Co_{0.5}S$//AC supercapattery. (b) Ragone plot of the various $Zn_xCo_{1-x}S$//AC devices.

sities, as depicted in Fig. 7(g). Fig. 7(h) shows the Nyquist plot of the $Zn_{0.5}Co_{0.5}S$//AC device in the frequency range of 0.01 Hz to 100 kHz, and fittings based on the equivalent circuit in the Fig. 7(h) inset yields an R_{ct} of 0.21 Ω and R_s of 0.59 Ω, again, the lowest among the series of samples.

In order to evaluate the service life of the $Zn_{0.5}Co_{0.5}S$//AC device, the cycle stability was probed at 10 A g^{-1} current density (Fig. 8(a)). After 10, 000 GCD cycles, the device retained around 88 % of the initial capacity, suggesting outstanding cycle stability. Note that for practical applications, energy density (E) and power density (P) also need to be taken into consideration. One can see that the $Zn_{0.5}Co_{0.5}S$//AC device achieved a high energy density of 49 Wh kg^{-1} at the power density of 957 W kg^{-1}, and even 23 Wh kg^{-1} when the energy density was increased by almost ten folds to 9413 W kg^{-1}. This performance is markedly higher than those of other $Zn_xCo_{1-x}S$//AC devices (Fig. S6).

The Ragone plot is depicted in Fig. 7(b), where the power and energy densities of the $Zn_{0.5}Co_{0.5}S$//AC device can be seen to be highly comparable to leading results in the literature based on relevant electrode materials, such as ZnCoS//PrGO (17.7 Wh kg^{-1} at 435 W kg^{-1}) [47], $ZnCo_2O_4$//AC (42.83 Wh kg^{-1} at 425 W kg^{-1}) [61], NiCoS//CC (33.4 Wh kg^{-1} at 751.5 W kg^{-1}) [62], CoS//CoS (14.25 Wh kg^{-1} at 150 W kg^{-1}) [63], $NiCo_2S_4$//C (22.8 Wh kg^{-1} at 160 W kg^{-1}) [64], $MnCo_2S_4$//PrOG (31.3 Wh kg^{-1} at 800 W kg^{-1}) [65], $CuCo_2S_4$//AC (40 Wh kg^{-1} at 379 W kg^{-1}) [66]. These observations suggest that the $Zn_{0.5}Co_{0.5}S$ nanosheets are viable electrode materials for the development of high-performance supercapatteries.

4. Conclusions

In summary, a series of porous $Zn_xCo_{1-x}S$ nanosheet arrays were prepared via a facile hydrothermal method. Of these, the $Zn_{0.5}Co_{0.5}S$ electrode displayed a high specific capacitance of 614 C g^{-1} at 1 A g^{-1} and excellent cycle retention rate of 90 % after 10, 000 cycles at 10 A g^{-1}, which were superior to other electrodes. Interestingly, the $Zn_{0.5}Co_{0.5}S$//AC supercapattery device also exhibited an excellent electrochemical performance, displaying a 49 Wh kg^{-1} energy density at 957 W kg^{-1} power density, and 23 Wh kg^{-1} at 9413 W kg^{-1}, as well as 88 % retention after 10, 000 cycles. This remarkable performance was attributed to the following structural characteristics: (i) the porous nanosheet morphology, (ii) the synergistic effect between the Co and Zn centers, and (iii) the various oxidation states in the ternary transition metal sulfides. Results from this work suggest that design and engineering of ternary transition metal sulfide nanosheets may be an effective route to the production of effective electrode materials for next-generation, high-performance energy storage technologies.

Declaration of Competing Interest

The authors declare no conflict of interest.

Acknowledgments

The authors gratefully acknowledge financial support from the National Natural Science Foundation of China (Nos. 21101176 and 21676036), the Fundamental Research Funds for the Central Universities of Chongqing University (Nos. 2018CDQYCH0028, 2018CDXYHG0028 and 2019CDXYHG0013), the Graduate Research and Innovation Foundation of Chongqing (No. CYS–20040), and the Large-scale Equipment Sharing Fund of Chongqing University (Nos. 201903150149 and 202003150020).

Appendix A. Supplementary data

Supplementary material related to this article can be found, in the online version, at doi:https://doi.org/10.1016/j.jmst.2021.01.085.

References

[1] A. Aricò, P. Bruce, B. Scrosati, J. Tarascon, W. van Schalkwijk, Nat. Mater. 4 (2005) 366–377.
[2] C. Liu, F. Li, L. Ma, H. Cheng, Adv. Mater. 22 (2010) E28–E62.
[3] P. Simon, Y. Gogotsi, Nat. Mater. 7 (2008) 845–854.
[4] L. Zhang, X. Zhao, Chem. Soc. Rev. 38 (2009) 2520–2531.
[5] G. Wang, L. Zhang, J. Zhang, Chem. Soc. Rev. 41 (2012) 797–828.
[6] H. Wang, H. Casalongue, Y. Liang, H. Dai, J. Am. Chem. Soc. 132 (2010) 7472–7477.
[7] W. Wei, X. Cui, W. Chen, D. Ivey, Chem. Soc. Rev. 40 (2011) 1697–1721.
[8] X. Xu, W. Shi, W. Liu, S. Ye, R. Yin, L. Zhang, L. Xu, M. Chen, M. Zhong, X. Cao, J. Mater. Chem. A 6 (2018) 24086–24091.
[9] M. Chen, H. Fan, Y. Zhang, X. Liang, Q. Chen, X. Xia,Small 16 (2020), 2003434.
[10] Q. Li, J. Zhou, R. Liu, L. Han, Dalton Trans. 48 (2019) 17163–17168.
[11] B. Huang, H. Wang, S. Liang, H. Qin, Y. Li, Z. Luo, C. Zhao, L. Xie, L. Chen, Energy Storage Mater. 32 (2020) 105–114.
[12] C. Yuan, L. Yang, L. Hou, L. Shen, X. Zhang, X. Lou, Energ. Environ. Sci. 5 (2012) 7883–7887.
[13] X. Zhang, W. Shi, J. Zhu, W. Zhao, J. Ma, S. Mhaisalkar, T. Maria, Y. Yang, H. Zhang, H. Hng, Q. Yan, Nano Res. 3 (2010) 643–652.
[14] S. Kim, J. Lee, H. Ahn, H. Song, J. Jang, ACS Appl. Mater. Inter. 5 (2013) 1596–1603.
[15] J. Yan, Z. Fan, T. Wei, W. Qian, M. Zhang, F. Wei, Carbon 48 (2010) 3825–3833.
[16] Y. He, G. Li, Z. Wang, C. Su, Y. Tong, Energ. Environ. Sci. 4 (2011) 1288–1292.
[17] X. Zhao, L. Mao, Q. Cheng, J. Li, F. Liao, G. Yang, L. Xie, C. Zhao, L. Chen,Chem. Eng. J. 387 (2020), 124081.
[18] J. Bhagwan, S. Rani, V. Sivasankaran, K. Yadav, Y. Sharma, Appl. Surf. Sci. 426 (2017) 913–923.
[19] M. Zhu, D. Meng, C. Wang, G. Diao, ACS Appl. Mater. Inter. 5 (2013) 6030–6037.
[20] L. Ren, J. Chen, X. Wang, M. Zhi, J. Wu, X. Zhang, RSC Adv. 5 (2015) 30963–30969.
[21] S. Xiong, H. Zeng, Angew. Chem. Int. Edit. 51 (2012) 949–952.
[22] M. Gao, Y. Xu, J. Jiang, S. Yu, Chem. Soc. Rev. 42 (2013) 2986–3017.
[23] Y. Wang, J. Wu, Y. Tang, X. Lü, C. Yang, M. Qin, F. Huang, X. Li, X. Zhang, ACS Appl. Mater. Inter. 4 (2012) 4246–4250.
[24] X. Chen, Q. Liu, T. Bai, W. Wang, F. He, M. Ye,Chem. Eng. J. (2020), 127237.
[25] X. Liang, Y. Li, H. Fan, S. Deng, X. Zhao, M. Chen, G. Pan, Q. Xiong, X. Xia,Nanotechnology 30 (2019), 484001.
[26] F. Yang, S. Deng, S. Lin, M. Chen, X. Xia, X. Lu,Nanotechnology 30 (2019), 404001.
[27] P. Zhang, Y. Liu, M. Zhou, Y. Xue, X. Zeng, J. Qi, M. Chen, F. Sun,Nanotechnology 31 (2020), 395401.

[28] S. Amaresh, K. Karthikeyan, I. Jang, Y. Lee, J. Mater. Chem. A 2 (2014) 11099–11106.
[29] C. Dai, P. Chien, J. Lin, S. Chou, W. Wu, P. Li, K. Wu, T. Lin, ACS Appl. Mater. Interfaces 5 (2013) 12168–12174.
[30] J. Xu, Q. Wang, X. Wang, Q. Xiang, B. Liang, D. Chen, G. Shen, ACS Nano 7 (2013) 5453–5462.
[31] X. Hou, T. Peng, J. Cheng, Q. Yu, R. Luo, Y. Lu, X. Liu, J. Kim, J. He, Y. Luo, Nano Res. 10 (2017) 2570–2583.
[32] F. Wu, J. Gao, X. Zhai, M. Xie, C. Gao, Y. Sun, Y. Liu, J. Yan, Electrochim. Acta 319 (2019) 859–868.
[33] I. Hussain, C. Lamiel, S. Mohamed, S. Vijayakumar, A. Ali, J. Shim, J. Ind. Eng. Chem. 71 (2019) 250–259.
[34] J. Wu, X. Shi, W. Song, H. Ren, C. Tan, S. Tang, X. Meng, Nano Energy 45 (2018) 439–447.
[35] J. Xiao, L. Wan, S. Yang, F. Xiao, S. Wang, Nano Lett. 14 (2014) 831–838.
[36] A. Elshahawy, X. Li, H. Zhang, Y. Hu, K. Ho, C. Guan, J. Wang, J. Mater. Chem. A 5 (2017) 7494–7506.
[37] J. Shen, J. Ji, P. Dong, R. Baines, Z. Zhang, P. Ajayan, M. Ye, J. Mater. Chem. A 4 (2016) 8844–8850.
[38] H. Chen, J. Jiang, L. Zhang, H. Wan, T. Qi, D. Xia, Nanoscale 5 (2013) 8879–8883.
[39] S. Attia, Y. Barakat, H. Hassan, S. Mohamed,J. Energy Storage 29 (2020), 101349.
[40] Y. Lv, A. Liu, Z. Shi, H. Che, J. Mu, Z. Guo, X. Zhang, Chem. Eng. J. 349 (2018) 397–407.
[41] B. Huang, W. Wang, T. Pu, J. Li, C. Zhao, L. Xie, L. Chen,Chem. Eng. J. 375 (2019), 121969.
[42] Y. Lu, Z. Li, Z. Bai, H. Mi, C. Ji, H. Pang, C. Yu, J. Qiu,Nano Energy 66 (2019), 104132.
[43] J. Yang, Y. Zhang, C. Sun, G. Guo, W. Sun, W. Huang, Q. Yan, X. Dong, J. Mater. Chem. A 3 (2015) 11462–11470.
[44] Y. Zhang, N. Cao, S. Szunerits, A. Addad, P. Roussel, R. Boukherroub, Chem. Eng. J. 374 (2019) 347–358.
[45] Z. Ji, N. Li, M. Xie, X. Shen, W. Dai, K. Liu, K. Xu, G. Zhu,Electrochim. Acta 334 (2020), 135632.
[46] H. Maruyama, H. Qiu, M. Hashimoto, K. Fudaba, H. Nakai, A. Barna, P. Barna, Thin Solid Films 299 (1997) 59–62.
[47] S. Thaiwatthana, N. Jantaping, P. Limthongkul, Surf. Eng. 28 (2012) 273–276.
[48] G. Greczynski, L. Hultman, Angew. Chem. Int. Edit. 59 (2020) 5002–5006.
[49] M. Zhang, Y. Sui, X. Yuan, J. Qi, F. Wei, Q. Meng, Y. He, Y. Ren, Z. Sun, J. Liu,Nano 14 (2019), 1950030.
[50] X. Wei, Y. Zhang, B. Zhang, Z. Lin, X. Wang, P. Hu, S. Li, X. Tan, X. Cai, W. Yang, L. Mai, Nano Energy 64 (2019) 103899.
[51] F. Hekmat, H. Hosseini, S. Shahrokhian, H. Unalan, Energy Storage Mater. 25 (2020) 621–635.
[52] M. Zhang, H. Fan, X. Ren, N. Zhao, H. Peng, C. Wang, X. Wu, G. Dong, C. Long, W. Wang, Y. Gao, L. Ma, P. Wu, H. Li, X. Jiang, J. Power Sources 418 (2019) 202–210.
[53] B. Wu, H. Qian, Z. Nie, Z. Luo, Z. Wu, P. Liu, H. He, J. Wu, S. Chen, F. Zhang, J. Energy Chem. 46 (2020) 178–186.
[54] X. Wang, R. Zhou, C. Zhang, S. Xi, M. Jones, T. Tesfamichael, A. Du, K. Gui, K. Ostrikov, H. Wang, J. Mater. Chem. A 8 (2020) 9278–9291.
[55] B. Huang, W. Wang, T. Pu, J. Li, J. Zhu, C. Zhao, L. Xie, L. Chen, J. Colloid Interf. Sci. 532 (2018) 630–640.
[56] Y. Li, Z. Luo, H. Qin, S. Liang, L. Chen, H. Wang, C. Zhao, S. Chen, J. Colloid Interf. Sci. 582 (2021) 842–851.
[57] J. Li, T. Pu, B. Huang, X. Hou, C. Zhao, L. Xie, L. Chen, J. Colloid Interf. Sci. 531 (2018) 360–368.
[58] N. Padmanathan, H. Shao, K. Razeeb, ACS Appl. Mater. Inter. 10 (2018) 8599–8610.
[59] H. Shao, N. Padmanathan, D. McNulty, C. O'Dwyer, K. Razeeb, ACS Appl. Energ. Mater. 2 (2019) 569–578.
[60] Q. Hu, M. Tang, M. He, N. Jiang, C. Xu, D. Lin, Q. Zheng,J. Power Sources 446 (2020), 227335.
[61] J. Zhu, D. Song, T. Pu, J. Li, B. Huang, W. Wang, C. Zhao, L. Xie, L. Chen, Chem. Eng. J. 336 (2018) 679–689.
[62] T. Liu, J. Liu, L. Zhang, B. Cheng, J. Yu, J. Mater. Sci. Technol. 47 (2020) 113–121.
[63] H. Wan, X. Ji, J. Jiang, J. Yu, L. Miao, L. Zhang, S. Bie, H. Chen, Y. Ruan, J. Power Sources 243 (2013) 396–402.
[64] W. Kong, C. Lu, W. Zhang, J. Pu, Z. Wang, J. Mater. Chem. A 3 (2015) 12452–12460.
[65] S. Liu, S.C. Jun, J. Power Sources 342 (2017) 629–637.
[66] Z. Wang, Z. Zhu, Q. Zhang, M. Zhai, J. Gao, C. Chen, B. Yang, Ceram. Int. 45 (2019) 21286–21292.